INORGANIC CHEMISTRY FRONTIERS

RESEARCH ARTICLE

View Article Online
View Journal | View Issue

Cite this: *Inorg. Chem. Front.*, 2023, **10**, 3714

Homochiral Cu_6Dy_3 single-molecule magnets displaying proton conduction and a strong magneto-optical Faraday effect†

Cai-Ming Liu, *[a] Shui-Dong Zhu,[b] Ying-Bing Lu, [b] Xiang Hao[a] and He-Rui Wen [c]

Received 7th April 2023,
Accepted 12th May 2023

DOI: 10.1039/d3qi00634d

rsc.li/frontiers-inorganic

Using the new Schiff base ligands condensed from 2-hydroxy-1-naphthalenecarboxaldehyde and (1*R*,2*R*)/(1*S*,2*S*)-2-aminocyclohexanol (*R*-H_3L/*S*-H_3L), a pair of homochiral Cu_6Dy_3 heterometallic cluster complexes $[Cu_6Dy_3(R\text{-L})_6(OH)_6(H_2O)_6](ClO_4)(NO_3)_2{\cdot}4.75H_2O{\cdot}8.5MeOH$ (*R*-**1**) and $[Cu_6Dy_3(S\text{-L})_6(OH)_6(H_2O)_6](ClO_4)(NO_3)_2{\cdot}5.5H_2O{\cdot}8MeOH$ (*S*-**1**) were synthesized at room temperature, which exhibit an interesting topology of triangular corner-sharing cubanes. Magnetic measurements revealed that they are zero-field single-molecule magnets (SMMs), with different U_{eff}/k values of 19.5(0.6) K for *R*-**1** and 21.4(0.4) K for *S*-**1**, owing to solvent magnetic effects. Meanwhile, the chiral enantiomers show proton conductivity caused by hydrogen bonding networks. Furthermore, the circular dichroism (CD) spectra of *R*-**1** and *S*-**1** confirmed their enantiomeric nature, and the magnetic circular dichroism (MCD) study indicated that both *R*-**1** and *S*-**1** have strong magneto-optical Faraday effects at room temperature, with a large $|g_{max(MCD)}|$ value of 0.58 T^{-1}.

Introduction

The integration of optical, electrical, magnetic and other functions in a nanoscale molecule can meet the requirements of micro-nano miniaturization and intelligent multi-signal responses in modern high-tech technology.[1] The advent of single-molecule magnets (SMMs)[2] is a crucial step towards achieving this goal. SMMs are molecular materials that can exhibit magnetic bistability in a single molecule at the nanoscale, so they are expected to be used to make molecular devices with high-density information storage.[3] When chirality is introduced into SMMs, it is possible to bring in many new valuable properties, such as ferroelectric properties,[4–8] second-order nonlinear optics,[9,10] magneto-optical Faraday effects,[11–13] magnetochiral dichroism (MChD),[14] *etc.*, to achieve the integration of multiple functions in a nanoscale molecule for future application. For example, SMMs with strong magneto-optical Faraday effects have potential applications not only in magneto-optical switches, isolators, or sensors, but also in optical current transformers,[12,13] and SMMs with strong MChD are further expected to be used for optical readout of magnetic data.[14] Furthermore, when there is a network of hydrogen bonds with the participation of crystalline water molecules, proton conductivity may be assigned in SMM systems,[15–18] while ferromagnetism and conductive bifunctions were once thought to be difficult to coexist in molecular systems,[19] and such magneto-conduction molecular materials have the potential to be used in low-consumption spintronic devices.[20] To date, only a few cases of conductive SMMs have been reported; they still require external dc field induction to exhibit magnetic relaxation behavior,[15–18] and there are only a few cases of SMMs with magneto-optical Faraday effects but they are not conductive.[11–13] It is a great challenge to obtain nanomolecules with integrated conductive, magnetic, and strong magneto-optical functions.

Lanthanide(III) ions have become important components for many SMMs,[21] especially for single-ion magnets (SIMs)[22–28] with large energy barrier values and high blocking

[a]*Beijing National Laboratory for Molecular Sciences, CAS Key Laboratory for Organic Solids, Institute of Chemistry, Chinese Academy of Sciences, Beijing 100190, China. E-mail: cmliu@iccas.ac.cn*

[b]*Jiangxi Key Laboratory of Function of Materials Chemistry, College of Chemistry and Chemical Engineering, Gannan Normal University, Ganzhou 341000, Jiangxi Province, China*

[c]*School of Metallurgy and Chemical Engineering, Jiangxi University of Science and Technology, Ganzhou 341000, Jiangxi Province, China*

†Electronic supplementary information (ESI) available: Selected bond lengths (Å) and angles (°) of *R*-**1** and *S*-**1**; continuous shape measure calculation for Dy(III) ions in *R*-**1** and *S*-**1**; the crystal structure of *S*-**1**; unit cell diagrams of *R*-**1** and *S*-**1**; *M versus H*/*T* and hysteresis loop plots for *R*-**1** and *S*-**1**; plots of ac magnetic susceptibility for *S*-**1**; MCD spectra of *R*-**1** and *S*-**1**; the proton conductivity of *R*-**1** and *S*-**1** under variable relative humidity (RH) and at 100% RH and variable temperature (°C); plots of proton conductivity for *S*-**1**. CCDC 2222613 and 2222614. For ESI and crystallographic data in CIF or other electronic format see DOI: https://doi.org/10.1039/d3qi00634d

temperatures because of their high spin ground state and magnetic anisotropy. Furthermore, they are also involved in the construction of many 3d–4f SMMs.[29] Among them, Dy–Cu SMMs can exhibit good magnetic relaxation properties without applying an external dc field,[30–37] but most of such SMMs reported in the literature are non-chiral. On the other hand, chiral SMMs with triangular Dy_3 structural units are particularly interesting because they can exhibit spin chirality as single-molecule toroics.[38] In this study, we are committed to constructing chiral 3d–4f multifunctional SMMs using new homochiral Schiff base ligands (*R*-H_3L/*S*-H_3L, Scheme 1), which are formed by the condensation reaction of 2-hydroxy-1-naphthalenecarboxaldehyde and (1*R*,2*R*)/(1*S*,2*S*)-2-aminocyclohexanol; such large π-conjugated homochiral ligands are expected to provide rich CD signals. Herein we report the syntheses, crystal structures, zero-field SMM behaviour, magneto-optical Faraday effects, and proton conduction properties of a pair of homochiral Cu–Dy multifunctional nanocluster complexes based on the *R*-H_3L/*S*-H_3L ligands, $[Cu_6Dy_3(R\text{-}L)_6(OH)_6(H_2O)_6](ClO_4)(NO_3)_2\cdot 4.75H_2O\cdot 8.5MeOH$ (*R*-**1**) and $[Cu_6Dy_3(S\text{-}L)_6(OH)_6(H_2O)_6](ClO_4)(NO_3)_2\cdot 5.5H_2O\cdot 8MeOH$ (*S*-**1**), which show an interesting topology of triangular corner-sharing cubanes.

Experimental

Materials and methods

All commercially available chemicals and solvents are analytically pure and not further purified prior to use.

Caution! Although there were no problems encountered in this work, perchlorate salts or complexes are potentially explosive; they should be handled with care and used only in small amounts.

The elemental analyses were carried out on a Thermo Flash EA1112 elemental analyzer. The infrared spectra were recorded on a Bruker VERTEX 70v spectrophotometer with pressed KBr pellets. The circular dichroism (CD) spectra and the magnetic circular dichroism (MCD) spectra were measured using a Chirascan ACD spectrometer, with a permanent magnet (+1.0 T or −1.0 T) and a 1 mm optical path. Proton conductivity measurements were carried out by a quasi-four-electrode AC impedance technique using a Solartron 1260 impedance/gain-phase analyzer, using the frequency domain of 10^6–0.1 Hz, the temperature range of 25 to 80 °C, and the relative humidity (RH) from 60 to 100%. The microcrystalline samples were compressed as pellets with 2.5 mm diameter and 0.62 mm thickness for *R*-**1** or 0.67 mm thickness for *S*-**1**; two sides of the pellet were connected to gold wires using gold paste. The resistance values were deduced from the Debye semicircle in the Nyquist plot, and the conductivities were calculated using the equation: $\sigma = L/(R \times A)$, where σ is the proton conductivity (S cm^{-1}), L is the thickness of the sample (cm), A is the cross-sectional area of the sample pellet (cm^2), and R is the resistance (Ω). The magnetic properties were determined on a Quantum Design MPMS-XL5 (SQUID) magnetometer. The diamagnetism of all constituent atoms was corrected using Pascal's constant.

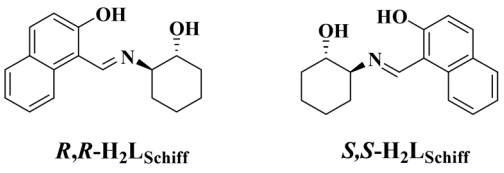

R,*R*-H_2L_{Schiff} *S*,*S*-H_2L_{Schiff}

Scheme 1 *R*,*R*-H_2L_{Schiff} and *S*,*S*-H_2L_{Schiff}.

Preparation of *R*,*R*-H_2L_{Schiff} and *S*,*S*-H_2L_{Schiff}

20 mmol of (1*R*,2*R*)/(1*S*,2*S*)-2-aminocyclohexanol and 20 mmol of 2-hydroxy-1-naphthalenecarboxaldehyde in 40 mL of MeOH were stirred for 24 hours at room temperature; a large amount of yellow turbidity appeared from the starting clear solution, and it was filtered, washed with EtOH and air-dried to give the product as a yellow powder.

Elemental analysis calcd (%) for $C_{17}H_{17}NO_2$ (*R*,*R*-H_2L_{Schiff}). C, 76.38; H, 6.41; N, 5.24; found: C, 76.43; H, 6.45; N, 5.21. IR (KBr, cm^{-1}): 3558 (m), 3481 (m), 3465(m), 3405(s), 3234(w), 3048(w), 2940(w), 2919(w), 2883(w), 2863(w), 1642(s), 1609(s), 1544(m), 1521(m), 1476(w), 1448(w), 1425(w), 1381(m), 1350(w), 1314(w), 1300(w), 1284(w), 1245(m), 1218(w), 1198(w), 1143(w), 1121(w), 1100(w), 1072(w), 1054(w), 1038(w), 881(w), 792(w), 693(w), 617(w), 479(w), 413(w).

Elemental analysis calcd (%) for $C_{17}H_{17}NO_2$ (*S*,*S*-H_2L_{Schiff}). C, 76.38; H, 6.41; N, 5.24; found: C, 76.33; H, 6.44; N, 5.20. IR (KBr, cm^{-1}): 3558 (m), 3481 (m), 3464(m), 3407(s), 3048(w), 2940(w), 2920(w), 2884(w), 2864(w), 1643(s), 1608(s), 1545(m), 1521(m), 1476(w), 1449(w), 1426(w), 1380(m), 1351(w), 1315(w), 1300(w), 1284(w), 1246(m), 1219(w), 1198(w), 1144(w), 1073(w), 1054(w), 1038(w), 881(w), 792(w), 694(w), 615(w), 479(w), 410(w).

Preparation of *R*-1 and *S*-1

0.125 mmol of $Dy(NO_3)_3\cdot 5H_2O$ was added to 0.25 mmol of *R*,*R*-H_2L_{Schiff} or *S*,*S*-H_2L_{Schiff} in 20 mL of MeOH; after stirring for 15 minutes, 0.25 mmol of $Cu(ClO_4)_2\cdot 6H_2O$ and 0.75 mmol of Et_3N were added in turn to the solution; blue-gray precipitates appeared quickly; 20 mL of CH_2Cl_2 was then added to the mixture to dissolve the precipitates. After being stirred for 24 hours, a dark blue solution was formed, and dark blue crystals of *R*-**1** or *S*-**1** were grown by slowly evaporating the solvent of this solution. After several days, the products were collected by filtration. High quality single crystals of both *R*-**1** or *S*-**1** could be obtained by recrystallization with the MeOH–CH_2Cl_2 (v/v: 1/1) mixed solvent. Yield: 75–80% based on Dy.

Elemental analysis calcd (%) for $C_{110.5}H_{163.5}N_8O_{47.25}ClCu_6Dy_3$ (*R*-1). C, 40.66; H, 5.05; N, 3.43; found: C, 40.53; H, 5.11; N, 3.41. IR(KBr, cm^{-1}): 3433 (br, s), 3062(w), 2930(w), 2856(w), 1625(s), 1543(m), 1510(w), 1455(w), 1435(w), 1387(m), 1362(w), 1339(m), 1298(w), 1245(w), 1186(w), 1166(w), 1147(w), 1117(w), 1093(w), 1053(w), 972(w), 921(w), 858(w), 828(w), 777(w), 747(w), 666(w), 629(w), 608(w), 549(w), 505(w), 464(w), 442(w).

Elemental analysis calcd (%) for $C_{110}H_{163}N_8O_{47.5}ClCu_6Dy_3$ (*S*-1). C, 40.51; H, 5.04; N, 3.44; found: C, 40.55; H, 5.09; N, 3.39. IR(KBr, cm^{-1}): 3426 (br, s), 3060(w), 2931(w), 2856(w), 1625(s), 1543(m), 1510(w), 1455(w), 1436(w), 1387(m), 1362(w), 1340(m), 1299(w), 1245(w), 1186(w), 1165(w), 1147(w), 1118(w), 1093(w), 1053(w), 972(w), 921(w), 858(w), 828(w), 778(w), 747(w), 710(w), 666(w), 630(w), 608(w), 550(w), 505(w), 445(w).

Crystallography

X-ray single crystal diffraction data for the two chiral isomers were collected on a Rigaku MM007HF diffractometer at 170 K using Mo-Kα radiation (λ = 0.71073 Å). The two structures were solved using the olex2.solve structure solution program and refined using the ShelXL-2015 refinement package. All non-hydrogen atoms were refined anisotropically, and all hydrogen atoms were treated as riding atoms. Crystallographic data are summarized in Table 1.

Results and discussion

Synthesis

Recently, the Schiff base ligands formed by the condensation reactions of 2-hydroxy-1-naphthaldehyde and achiral hydroxylamine have been successfully used to assemble several achiral Ln–Ni cluster complexes (including a Dy_3Ni_3 SMM)[39] and several achiral Dy–Co cluster SMMs under hydrothermal conditions.[40] We hope to construct chiral 3d–4f SMMs using the homochiral Schiff base ligands derived from 2-hydroxy-1-naphthaldehyde, as these large π-conjugated homochiral ligands may provide rich CD signals. We pre-synthesized a series of homochiral Schiff base ligands by the condensation reaction of 2-hydroxy-1-naphthaldehyde and several homochiral hydroxylamines, and finally found that the homochiral Cu_3Dy_6 cluster complexes *R*-**1** and *S*-**1** could be reproducibly synthesized by the reaction of the homochiral Schiff base ligands *R*-H_3L/*S*-H_3L (shown in Scheme 1) with $Dy(NO_3)_3{\cdot}5H_2O$ and $Cu(ClO_4)_2{\cdot}6H_2O$ in the MeOH–CH_2Cl_2 (v/v: 1/1) mixed solvent in the presence of triethylamine at room temperature. The use of a room-temperature reaction instead of a high-temperature hydrothermal reaction can effectively avoid the occurrence of a racemic mixture of the product.[41] Notably, although CH_2Cl_2 is not present in the crystal lattices of *R*-**1** and *S*-**1**, it is essential for growing these homochiral Cu_3Dy_6 cluster complexes' single crystals, and when it is replaced with other solvents such as MeCN, the crystalline product cannot be obtained at all. Notably, although homochiral SMMs have been continuously exploited,[4–14,42–44] *R*-**1** and *S*-**1** are very rare homochiral Cu–Dy multinuclear cluster-type SMMs. Furthermore, a review of the latest CCDC database shows that *R*-**1** and *S*-**1** represent the first complexes assembled with the homochiral Schiff base ligands derived from 2-hydroxy-1-naphthalenecarboxaldehyde and (1*R*,2*R*)/(1*S*,2*S*)-2-aminocyclohexanol.

Table 1 Crystal data and structural refinement parameters for two enantiomers *R*-**1** and *S*-**1**

	R-**1**	*S*-**1**
Formula	$C_{110.5}H_{163.5}ClCu_6Dy_3N_8O_{47.25}$	$C_{110}H_{163}N_8O_{47.5}ClCu_6Dy_3$
F_W	3264.17	3261.66
Crystal system	Orthorhombic	Orthorhombic
Space group	$P2_12_12_1$	$P2_12_12_1$
a [Å]	17.5288(2)	17.6273(2)
b [Å]	22.4741(2)	22.5554(2)
c [Å]	35.9503(3)	35.9679(3)
α [°]	90	90
β [°]	90	90
γ [°]	90	90
V [Å^3]	14 162.4(2)	14 300.5(2)
Z	4	4
ρ_{calc}[g·cm^{-3}]	1.531	1.515
μ[mm^{-1}]	2.543	2.518
T [K]	170	170
λ [Å]	0.71073	0.71073
Reflections collected	113 383	285 418
Unique reflections	27 906	39 750
Observed reflections	26 474	36 891
Parameters	1642	1621
GoF[$I \geq 2\sigma(I)$]	1.075	1.135
R_1[$I \geq 2\sigma(I)$]	0.0324	0.0377
wR_2[$I \geq 2\sigma(I)$]	0.0888	0.0973
Flack value	−0.019(2)	−0.008(2)
CCDC	2222613	2222614

Crystal structures

Single crystal structure investigation of the two chiral isomers reveals that the Flack values of *R*-**1** and *S*-**1** are −0.019(2) and −0.008(2) (Table 1), respectively, which are close to zero, verifying the enantiomeric purity of their single crystals. Given that the structures of *R*-**1** and *S*-**1** are very similar, we only carefully describe the structure of *R*-**1**. As shown in Fig. 1a, the main body of the *R*-**1** molecule is composed of a heterometallic cluster cation $[Cu_6Dy_3(R\text{-}L)_6(OH)_6(H_2O)_6]^{3+}$, two nitrate anions and one perchlorate anion. In addition, *R*-**1** also contains some lattice water and methanol molecules in its crystal structure (Fig. S1†). The core of $[Cu_6Dy_3(R\text{-}L)_6(OH)_6]$ is made up of three $Cu_2Dy_2O_4$ twisted cubanes by sharing three Dy^{3+} vertices, generating an interesting topology of triangular corner-sharing cubanes (Fig. 1b). Such a topology is reminiscent of that in the achiral Dy_3Cu_6 complex $[Cu_6Dy_3(OH)_6(vae)_6(MeOH)(H_2O)_5]Br_2{\cdot}NO_3{\cdot}MeOH{\cdot}4H_2O$ {H_2vae = (2-[(3-hydroxy-ethylimino)-methyl]-6-methoxy-phenol)},[33] whose cation is $[Cu_6Dy_3(OH)_6(vae)_6(MeOH)(H_2O)_5]^{3+}$, containing five coordinated H_2O molecules and one coordinated MeOH molecule, while the cation $[Cu_6Dy_3(R\text{-}L)_6(OH)_6(H_2O)_6]^{3+}$ in *R*-**1** has only six coordinated H_2O molecules. The Dy1···Dy2, Dy2···Dy3 and Dy3···Dy1 distances in *R*-**1** are 3.851, 3.846, and 3.851(4) Å, respectively. The average Dy–O distance of 2.374 Å (Table S1†) is within the normal range.[21] The $Cu_2Dy_2O_4$ cubane in *R*-**1** is formed by two outer μ^3-O_{alkyl} groups from two *R*-L^{2-} ligands and two inner μ^3-OH groups bridging two inner Dy^{3+} cations

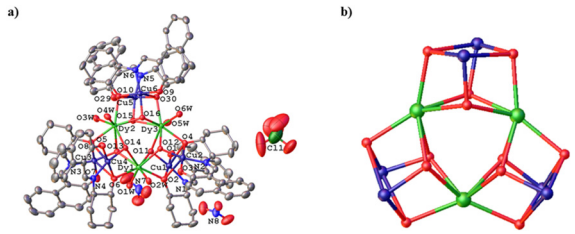

Fig. 1 Crystal structure of *R*-**1**; all H atoms and solvent molecules are omitted for clarity (a). Corner-sharing $[Cu_6Dy_3(R\text{-}L)_6(OH)_6]$ cubanes (b).

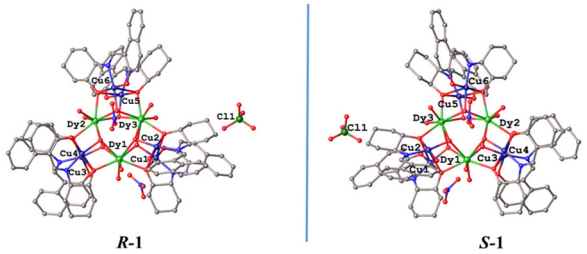

Fig. 2 Mirror symmetry of *R*-**1** and *S*-**1**.

with two outer Cu^{2+} cations (Fig. 1a), with the Cu···Cu distances of 3.154, 3.163, and 3.121 Å for Cu1···Cu2, Cu3···Cu4, and Cu5···Cu6, respectively.

Each Cu(II) cation is five-coordinated and shows a distorted square pyramidal coordination configuration, in which the O_{alkyl} atom, the $O_{phenoxide}$ atom and the N_{imine} atom from the same *R*-L^{2-} ligand and one $O_{hydroxyl}$ atom generate the square bottom, while the O_{alkyl} atom of the neighboring *R*-L^{2-} ligand acts as the apex. The twisting parameter τ could be calculated using the formula $\tau = (\beta - \alpha)/60$ ($\beta \geq \alpha$),[45] giving the τ values of 0.002 for Cu1, 0.150 for Cu2, 0.188 for Cu3, 0.138 for Cu4, 0.142 for Cu5, and 0.032 for Cu6. The smaller the τ value, the closer it is to the standard square pyramidal configuration. It can be seen that in each $Cu_2Dy_2O_4$ cubane, there is one Cu(II) cation (Cu1, Cu4 or Cu6) that is closer to the standard square pyramidal configuration than the other Cu(II) cation (Cu2, Cu3 or Cu5). Each Dy(III) ion is bonded to two O_{alkyl} atoms from two *R*-L^{2-} ligands, four $O_{hydroxyl}$ atoms and two O_{water} atoms. Through the SHAPE software analysis,[46] it is known that the coordination geometry of Dy1, Dy2 and Dy3 cations is the square antiprism configuration, with the offset values of 0.890, 0.672 and 0.606, respectively, for the D_{4d} symmetry (Tables S1–S3†).

The cation $[Cu_6Dy_3(R\text{-}L)_6(OH)_6(H_2O)_6]^{3+}$ in *R*-**1** is charge-balanced by two NO_3^- anions and one ClO_4^- anion. Notably, the crystal lattice contains some water and methanol molecules that participate in and form extensive hydrogen bonds among the molecules (Fig. S1†). This hydrogen bond network not only stabilizes the crystal structure, but also facilitates proton conduction in the solid phase.

The structure of *S*-**1** (Fig. S2 and Fig. S3†) is similar to that of *R*-**1** (Fig. 1 and Fig. S1†). The mean Dy–O distance of *S*-**1** is 3.377 Å (Table S1†), which is comparable to 3.374 Å of *R*-**1**. Similarly, the SHAPE software analysis[46] revealed that the coordination geometry of the Dy1, Dy2 and Dy3 cations of *S*-**1** is the square antiprism configuration too, with the offset values of 0.859, 0.713 and 0.569, respectively, for the D_{4d} symmetry (Tables S5–S7†), and the τ values of *S*-**1** were calculated to be 0.013 for Cu1, 0.138 for Cu2, 0.190 for Cu3, 0.135 for Cu4, 0.143 for Cu5, and 0.023 for Cu6. Because *R*-**1** and *S*-**1** are a pair of enantiomers, their principal structures are mirror-symmetrical (Fig. 2). Notably, the numbers of methanol solvent molecules and water solvent molecules contained in *S*-**1** are somewhat different from those in *R*-**1**, however, similar to *R*-**1**, there are extensive hydrogen bonds in the crystal structure of *S*-**1** involving crystal water and methanol molecules (Fig. S3†).

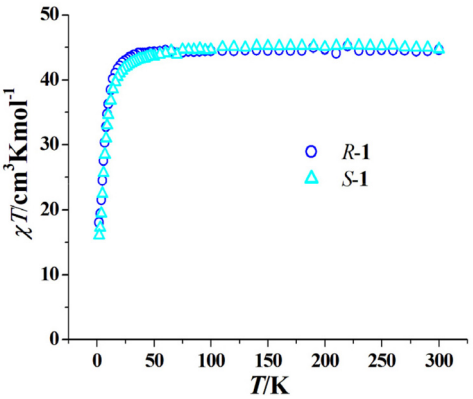

Fig. 3 Plots of χT *versus* *T* of *R*-**1** and *S*-**1** (H_{dc} = 1000 Oe).

Magnetic properties

The magnetic properties of *R*-**1** and *S*-**1** are similar since they are a pair of enantiomers; therefore, we only describe the magnetic properties of *R*-**1** in detail. As shown in Fig. 3, the room temperature χT values of *R*-**1** and *S*-**1** are 44.68 and 44.70 cm^3 K mol^{-1}, respectively, both are consistent with the calculated value (44.76 cm^3 K mol^{-1}) of three isolated Dy(III) ions and six uncoupling Cu(II) ions. When the temperature is decreased, the χT values of *R*-**1** and *S*-**1** slowly decrease, and rapidly decrease below 50 K to 15.74 cm^3 K mol^{-1} for *R*-**1** and 16.06 cm^3 K mol^{-1} for *S*-**1** at 2 K. A similar trend was observed in the achiral Cu_6Dy_3 Schiff base complex $[Cu_6Dy_3(OH)_6(vae)_6(MeOH)(H_2O)_5]Br_2{\cdot}NO_3{\cdot}MeOH{\cdot}4H_2O$ with the similar topology core,[33] and this magnetic behaviour can be explained by the depopulation of the m_J levels of dysprosium(III) cations and/or the antiferromagnetic coupling among cations.[33] The field-dependent magnetization of *R*-**1** and *S*-**1** was measured in the 2–6 K temperature range, and the corresponding *M versus* *H*/*T* curves at different temperatures do not coincide (Fig. S4 and Fig. S5†), suggesting the presence of magnetic anisotropy, which is one important prerequisite for SMMs.

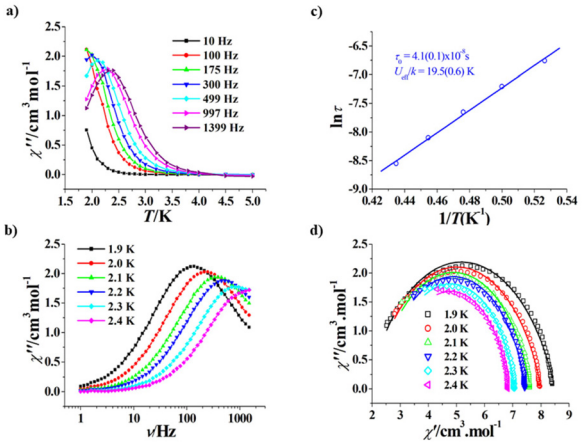

Fig. 4 Plots of χ'' *versus* T for *R*-**1** (H_{dc} = 0 Oe) (a). Frequency dependence of χ'' for *R*-**1** at a zero dc field (b). Plot of $-\ln(\tau)$ *versus* $1/T$ for *R*-**1** (H_{dc} = 0 Oe); the solid line represents the best fitting with the Arrhenius law (c). Cole–Cole plots measured from 1.9 to 2.4 K for *R*-**1** (H_{dc} = 0 Oe); the solid lines represent the best fitting with the generalized Debye model (d).

To further disclose the SMM behaviour of *R*-**1**, we measured its variable temperature ac magnetic susceptibility and variable frequency ac magnetic susceptibility at a zero dc field. As shown in Fig. 4a, the χ'' *versus* T plots at different frequencies (10–1399 Hz) clearly exhibit frequency dependence, suggesting the magnet relaxation behaviour of the SMM. Peaks occur on the curves from 300 Hz to 1399 Hz, and the Φ value was calculated to be 0.25 for *R*-**1** using the equation $\Phi = (\Delta T_f/T_f)/\Delta(\log f)$ (f is the frequency);[47] this value is obviously larger than that for the spin glass state (<0.1), confirming the SMM nature of magnetic relaxation. The χ'' *versus* ν plots at 1.9–2.4 K also display frequency dependence and peaks occur on the curves from 1.9 K to 2.3 K (Fig. 4b). The extracted $\ln\tau$ *versus* $1/T$ plot follows the Arrhenius law $\tau = \tau_0 \exp(U_{eff}/kT)$ (Fig. 4c), with U_{eff}/k = 19.5(0.6) K and $\tau_0 = 4.1(0.1) \times 10^{-8}$ s. The τ_0 value is a normal value for SMMs.[21] In addition, the Cole–Cole plots show a typical single magnetic relaxation process, and were fitted by a generalized Debye model (Fig. 4d),[48,49] giving the α values of 0.119–0.222, suggesting that the relaxation time distribution of *R*-**1** is relatively narrow. However, *R*-**1** has no obvious hysteresis loop at 1.9 K (Fig. S6†).

The ac magnetic susceptibility of *S*-**1** is similar to that of *R*-**1**, as shown in Fig. S7a;† frequency dependence occurs on the χ'' *versus* T plots but peaks appear on the curves from 175 Hz to 1399 Hz. The Φ value of *S*-**1** was calculated to be 0.22, which is a little smaller than that of *R*-**1** (0.25), but also a normal value for SMMs. Frequency dependence can also be seen in the χ'' *versus* ν plots at 1.9–2.5 K of *S*-**1** and peaks occur on the curves from 1.9 K to 2.4 K (Fig. S7b†). The $\ln\tau$ *versus* $1/T$ plot of *S*-**1** was also fitted by the Arrhenius law $\tau = \tau_0 \exp(U_{eff}/kT)$ (Fig. S7c†), giving U_{eff}/k = 21.4(0.4) K and $\tau_0 = 2.7(0.1) \times 10^{-8}$ s. The U_{eff}/k value of *S*-**1** (21.4 K) is slightly larger than that of *R*-**1** (19.5 K), but a little smaller than that of the achiral complex $[Cu_6Dy_3(OH)_6(vae)_6(MeOH)(H_2O)_5]Br_2{\cdot}NO_3{\cdot}MeOH{\cdot}4H_2O$ (25.3 K).[33] As mentioned above, there is a difference in the numbers of methanol solvent molecules and water solvent molecules contained in *S*-**1** and *R*-**1**, which may cause subtle differences in their SMM properties due to solvent magnetic effects. Similar solvent magnetic effects of SMMs are also observed in other 3d–4f molecular systems.[34,50] However, the solvent magnetic effects in chiral SMMs have rarely been reported before.[51] The Cole–Cole plots of *S*-**1** could also be fitted by a generalized Debye model (Fig. S7d†),[48,49] giving the α values in the range of 0.115–0.249. Similar to *R*-**1**, no hysteresis loop can be formed for *S*-**1** at 1.9 K (Fig. S8†).

Circular dichroism (CD) spectra and magnetic circular dichroism (MCD) properties

The optical activity and chiral enantiomeric nature of *R*-**1** and *S*-**1** were confirmed with their circular dichroism (CD) spectra. As shown in Fig. 5a, the CD signal curves of *R*-**1** and *S*-**1** in an acetonitrile solution at a concentration of 0.2 g L^{-1} show mirror symmetry in the range of 250–700 nm, with strong peaks at 270, 316 and 398 nm, respectively, and a weak peak at around 572 nm. Referring to the UV-visible spectra (Fig. 5b), the CD peak at 270 nm is ascribed to the π–π* transitions of naphthalene rings in the homochiral Schiff base ligands, while the CD peaks at 316 nm and 398 nm are attributed to the π–π* transition and n–π* transition of the azomethylene chromatophores of the homochiral Schiff base ligands, respectively. Furthermore, the weak peak at 572 nm may be caused by the d–d transition of the Cu^{2+} cation.

We further studied the magneto-optical Faraday effects of *R*-**1** and *S*-**1** by measuring their MCD spectra in a MeCN solution (0.2 g L^{-1}) at room temperature with a 1 mm optical path. As shown in Fig. 5c, although the external magnetic field (± 1.0 T) basically does not change the position of the CD signal peak, it does change the strength of the signal clearly. The pure MCD signals of *R*-**1** and *S*-**1** were obtained based on

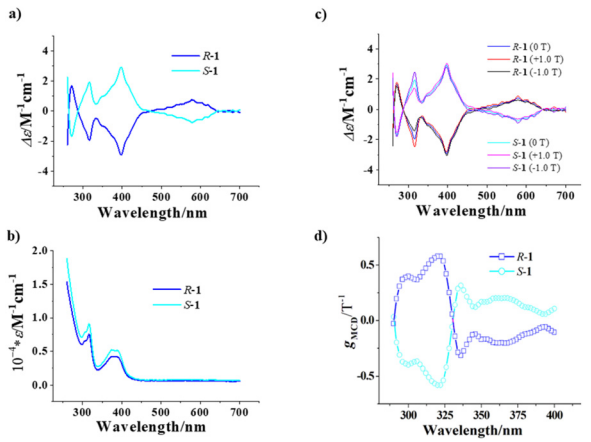

Fig. 5 CD spectra of *R*-**1** and *S*-**1** at room temperature (MeCN, c = 0.2 g L^{-1}, optical path = 1 mm) (a). UV-visible spectra of *R*-**1** and *S*-**1** at room temperature (MeCN, c = 0.2 g L^{-1}, optical path = 1 mm) (b). CD spectra in a MeCN solution at room temperature (c = 0.2 g L^{-1}, optical path = 1 mm, H = 0 and ± 1.0 T) (c). g_{MCD} of *R*-**1** and *S*-**1** (d).

the formula MCD = [CD(+1.0 T) − CD(−1.0 T)]/2,[12,13] and show a strong peak at 316 nm (Fig. S9†) attributed to the π–π* transitions of naphthalene rings in the homochiral Schiff base ligands.

To figure out the strength of the magneto-optical Faraday effects of *R*-**1** and *S*-**1**, we calculated the g_{MCD} (the anisotropy factor of MCD) values using the formula $g_{MCD} = 2(\varepsilon_+(B) - \varepsilon_+(-B))/(\varepsilon_+(B) + \varepsilon_+(-B))$.[52] As shown in Fig. 5d, the g_{MCD} values of *R*-**1** and *S*-**1** are also approximately mirror-symmetrical as a function of wavelength in the 290–400 nm range. The $g_{max(MCD)}$ values of *R*-**1** and *S*-**1** are 0.58 T^{-1} and −0.58 T^{-1}, respectively; their absolute values (both are 0.58 T^{-1}) are clearly larger than those of other reported 3d–4f complexes $[Co_2Ln[(R)/(S)\text{-}L]_4]\cdot Cl_5\cdot 2H_2O\cdot MeOH\cdot EtOH$ (Ln = Gd, Dy) (0.02 T^{-1})[53] and $\{[Mn_{10}Dy_6(L1)_2(R/S\text{-}L2)_6Ac_{12}(\mu^3\text{-}OH)_6(\mu^5\text{-}O)(\mu^4\text{-}O)_6(\mu^2\text{-}H_2O)_2]\}\{[Mn_6Dy_2(L1)_2(R/S\text{-}L2)_6Ac_2(\mu^4\text{-}O)_2(\mu^3\text{-}OH)_2(H_2O)_2]\}\cdot 4ClO_4\cdot EtOH\cdot 10H_2O$ (HL1 = 2-hydroxy-4-methoxybenzaldehyde; H_2L2 = (*R*/*S*)-2-(((1-hydroxybutan-2-yl)imino) methyl)-5-methoxyphenol) (0.012 T^{-1}),[12] and most of the 4f complexes (≤0.24 T^{-1}),[54] and are just smaller than those of a pair of homochiral Dy_2 complexes reported by our group recently (1.27 and 1.72 T^{-1}).[13] To our knowledge, the absolute values of $g_{max(MCD)}$ of *R*-**1** and *S*-**1** are the highest among those of the complex-type molecular materials; such large absolute values of $|g_{max(MCD)}|$ suggest that *R*-**1** and *S*-**1** possess strong magneto-optical Faraday effects. Because g_{MChD} is proportional to g_{MCD},[53] the homochiral Cu_6Dy_3 SMMs may also have larger g_{MChD} values.

Proton conductivity

Due to the presence of extensive hydrogen bonds in the crystal lattices of both *R*-**1** and *S*-**1** containing crystalline water molecules (Fig. S1 and Fig. S3†), their proton conductive properties in solid states were explored. As shown in Fig. 6, the Nyquist plots of *R*-**1** have a typical proton transfer characteristic,[55–66] consisting of a semicircle in the low-frequency region connecting with an inclined tail in the high-frequency region (Fig. 6a and b). At 25 °C, the proton conductivity value of *R*-**1** increases from 5.85 × 10^{-8} S cm^{-1} at 60% relative humidity to 9.55 × 10^{-7} S cm^{-1} at 100% relative humidity (Fig. 6c and Table S8†), which is consistent with the general regularity of solid-state proton conductivity increasing with the increase of relative humidity.[55–66]

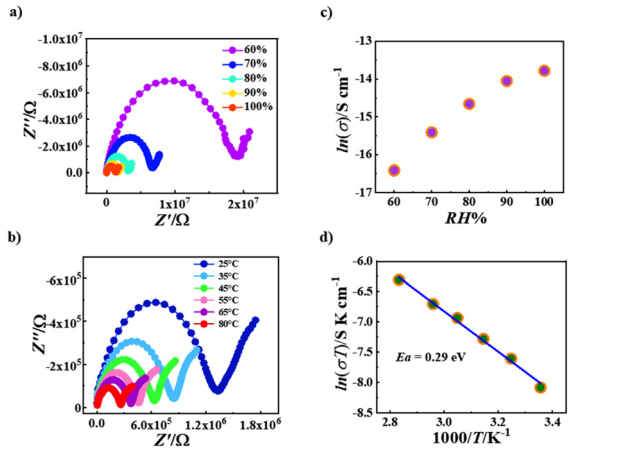

Fig. 6 Nyquist plots for *R*-**1** at 25 °C under different relative humidity (RH) levels (a). Nyquist plots for *R*-**1** at different temperatures under 100% relative humidity (RH) (b). Plots of proton conductivity *vs.* RH for *R*-**1** at 25 °C (c). Plots of ln(*σT*) *vs.* 1000/*T* for *R*-**1** under 100% relative humidity (RH) (d).

On the other hand, the temperature has also a significant effect on the proton conductivity; the higher the temperature, the better the proton conduction in the solid phase.[55–66] As shown in Fig. 6b, when the relative humidity is fixed at 100%, the proton conductivity of *R*-**1** increases from 9.55 × 10^{-7} S cm^{-1} at 25 °C to 4.77 × 10^{-6} S cm^{-1} at 80 °C (Table S9†). The maximum value of *R*-**1** at 100% RH and 80 °C is comparable with those of recently explored proton-conducting molecular materials, such as UiO-66-NH 2 (3.5 × 10^{-6} S cm^{-1} at 98% RH and 80 °C)[67] and GTUB5(3.00 × 10^{-6} S cm^{-1} at 75% RH and 75 °C).[68] Generally, the mechanism of the proton transport process can be judged according to the magnitude of the activation energy (E_a): when E_a < 0.4 eV, the Grotthuss mechanism is mainly mediated along the hydrogen bond network through proton jumping; conversely, when E_a > 0.4 eV, the carrier mechanism is mainly mediated by the proton diffusion of movable species.[55–66] We fitted the ln(*σT*) *vs.* 1000/*T* data with the formula $\sigma T = A\exp(-E_a/kT)$, giving the E_a value of 0.29 eV for *R*-**1** (Fig. 6d), which is obviously smaller than 0.4 eV, suggesting that *R*-**1** undergoes proton transfer through the Grotthuss mechanism. This is consistent with the presence of extensive hydrogen bonds in *R*-**1** involving crystalline water molecules.

The proton conductive properties of *S*-**1** (Fig. S10†) are similar to those of *R*-**1** (Fig. 6). At 25 °C, the proton conductivity value of *S*-**1** increases from 3.57 × 10^{-9} S cm^{-1} at 60% relative humidity to 2.40 × 10^{-7} S cm^{-1} at 100% relative humidity (Fig. S10a, Fig. S10c and Table S10†); on the other hand, at 100% relative humidity, the proton conductivity of *S*-**1** increases from 2.40 × 10^{-7} S cm^{-1} at 25 °C to 7.45 × 10^{-7} S cm^{-1} at 80 °C (Fig. S10b and Table S11†). The maximum value of *S*-**1** at 100% RH and 80 °C (7.45 × 10^{-7} S cm^{-1}) (Table S11†) is smaller than that of *R*-**1** (4.77 × 10^{-6} S), suggesting that the hydrogen bond network in *S*-**1** is less efficient at transporting protons with respect to that in *R*-**1**. The difference in their hydrogen bond networks is obviously caused by the difference in the numbers of methanol solvent molecules and water solvent molecules. The E_a value of *S*-**1** was calculated to be 0.22 eV using the formula $\sigma T = A\exp(-E_a/kT)$ again (Fig. S10d†), which is also smaller than 0.4 eV, confirming the Grotthuss mechanism for the proton transport process in *S*-**1**.

Conclusion

In summary, we successfully constructed the first homochiral 3d–4f cluster complexes using the new 2-hydroxy-1-naphthalenecarboxaldehyde-based homochiral Schiff base ligands,

$[Cu_6Dy_3(R\text{-}L)_6(OH)_6(H_2O)_6](ClO_4)(NO_3)_2\cdot 4.75H_2O\cdot 8.5MeOH$ (*R*-**1**) and $[Cu_6Dy_3(S\text{-}L)_6(OH)_6(H_2O)_6](ClO_4)(NO_3)_2\cdot 5.5H_2O\cdot 8MeOH$ (*S*-**1**), exhibiting zero-field SMM performance and a strong magneto-optical Faraday effect with a larger $|g_{max(MCD)}|$ value of 0.58 T^{-1}. In addition, they exhibit proton conductivity, thanks to the extensive hydrogen bonds associated with water solvent molecules in the crystal lattice. The two Cu_6Dy_3 chiral isomers not only integrate magnetism and conductivity, but also can realize the strong coupling of magneto-optical properties, showing a strong magneto-optical Faraday effect. This work demonstrates that 2-hydroxy-1-naphthalenecarboxaldehyde-based homochiral Schiff base ligands are excellent multidentate ligands for the assembly of homochiral 3d–4f multifunctional SMMs, magnetism and conductivity can be integrated into nanoscale homochiral 3d–4f molecules, and even strong coupling of magneto-optical properties can be achieved.

Conflicts of interest

There are no conflicts to declare.

Acknowledgements

This research was made possible by a generous grant from the National Natural Science Foundation of China (Grant Numbers 21871274 and 22271289).

References

1 J. Long, M. S. Ivanov, V. A. Khomchenko, E. Mamontova, J. M. Thibaud, J. Rouquette, M. Beaudhuin, D. Granier, R. A. S. Ferreira, L. D. Carlos, B. Donnadieu, M. S. C. Henriques, J. A. Paixao, Y. Guari and J. Larionova, Room temperature magnetoelectric coupling in a molecular ferroelectric ytterbium(III) complex, *Science*, 2020, **367**, 671.

2 R. Sessoli, D. Gatteschi, A. Caneschi and M. A. Novak, Magnetic Bistability in a Metal-Ion Cluster, *Nature*, 1993, **365**, 141.

3 D. Gatteschi and R. Sessoli, Quantum Tunneling of Magnetization and Related Phenomena in Molecular Materials, *Angew. Chem., Int. Ed.*, 2003, **42**, 268.

4 D.-P. Li, T.-W. Wang, C.-H. Li, D.-S. Liu, Y.-Z. Li and X.-Z. You, Single-ion magnets based on mononuclear lanthanide complexes with chiral Schiff base ligands [Ln$(FTA)_3$L] (Ln=Sm, Eu, Gd, Tb and Dy), *Chem. Commun.*, 2010, **46**, 2929.

5 X.-L. Li, C.-L. Chen, Y.-L. Gao, C.-M. Liu, X.-L. Feng, Y.-H. Gui and S.-M. Fang, Modulation of Homochiral Dy^{III} Complexes: Single-Molecule Magnets with Ferroelectric Properties, *Chem. – Eur. J.*, 2012, **18**, 14632.

6 X.-L. Li, M. Hu, Z. Yin, C. Zhu, C.-M. Liu, H.-P. Xiao and S. Fang, Enhanced single-ion magnetic and ferroelectric properties of mononuclear Dy(III) enantiomeric pairs through the coordination role of chiral ligands, *Chem. Commun.*, 2017, **53**, 3998.

7 P.-H. Guo, J.-L. Liu, J.-H. Jia, J. Wang, F.-S. Guo, Y.-C. Chen, W.-Q. Lin, J.-D. Leng, D.-H. Bao, X.-D. Zhang, J.-H. Luo and M.-L. Tong, Multifunctional Dy_4^{III} Cluster Exhibiting White-Emitting, Ferroelectric and Single-Molecule Magnet Behavior, *Chem. – Eur. J.*, 2013, **19**, 8769.

8 R. Akiyoshi, H. Zenno, Y. Sekine, M. Nakaya, M. Akita, D. Kosumi, L. F. Lindoy and S. Hayami, A Ferroelectric Metallomesogen Exhibiting Field-Induced Slow Magnetic Relaxation, *Chem. – Eur. J.*, 2022, **28**, e202103367.

9 H.-R. Wen, J.-J. Hu, K. Yang, J.-L. Zhang, S.-J. Liu, J.-S. Liao and C.-M. Liu, Family of Chiral Zn^{II}-Ln^{III} (Ln=Dy and Tb) Heterometallic Complexes Derived from the Amine-Phenol Ligand Showing Multifunctional Properties, *Inorg. Chem.*, 2020, **59**, 2811.

10 C.-M. Liu, R. Sun, B.-W. Wang, X. Hao and X.-L. Li, Effects of Counterions, Coordination Anions, and Coordination Solvent Molecules on Single-Molecule Magnetic Behaviors and Nonlinear Optical Properties of Chiral Zn_2Dy Schiff Base Complexes, *Inorg. Chem.*, 2022, **61**, 18510.

11 K. Wang, S. Zeng, H. Wang, J. Dou and J. Jiang, Magneto-chiral dichroism in chiral mixed (phthalocyaninato)(porphyrinato) rare earth triple-decker SMMs, *Inorg. Chem. Front.*, 2014, **1**, 167.

12 X. Wang, M.-H. Du, H. Xu, L.-S. Long, X.-J. Kong and L.-S. Zheng, Cocrystallization of Chiral 3d-4f Clusters $\{Mn_{10}Ln_6\}$ and $\{Mn_6Ln_2\}$, *Inorg. Chem.*, 2021, **60**, 5925.

13 C.-M. Liu, R. Sun, B.-W. Wang, F. Wu, X. Hao and Z. Shen, Homochiral Ferromagnetic Coupling Dy_2 Single-Molecule Magnets with Strong Magneto-Optical Faraday Effects at Room Temperature, *Inorg. Chem.*, 2021, **60**, 12039.

14 M. Atzori, K. Dhbaibi, H. Douib, M. Grasser, V. Dorcet and I. B. Breslavetz, Helicene-Based Ligands Enable Strong Magneto-Chiral Dichroism in a Chiral Ytterbium Complex, *J. Am. Chem. Soc.*, 2021, **143**, 2671.

15 S.-D. Zhu, J.-J. Hu, L. Dong, H.-R. Wen, S.-J. Liu, Y.-B. Lu and C.-M. Liu, Multifunctional Zn(ii)–Yb(iii) complex enantiomers showing second-harmonic generation, near-infrared luminescence, single-molecule magnet behaviour and proton conduction, *J. Mater. Chem. C*, 2020, **8**, 16032.

16 S.-D. Zhu, L. Dong, J.-J. Hu, H.-R. Wen, Y.-B. Lu, W.-H. Deng, C.-M. Liu, S.-J. Liu, G. Xu and Z.-H. Fu, A proton conductor showing an indication of single-ion magnet behavior based on a mononuclear Dy(iii) complex, *J. Mater. Chem. C*, 2021, **9**, 481.

17 D. Shao, W.-J. Tang, Z. Ruan, X. Yang, L. Shi, X.-Q. Wei, Z. Tian, K. Kumaric and S. K. Singh, Water-driven reversible switching of single-ion magnetism and proton conduction in a dysprosium sulfonate, *Inorg. Chem. Front.*, 2022, **9**, 6147.

18 Y.-B. Lu, J. Huang, Y.-Q. Liao, X.-L. Lin, S.-Y. Huang, C.-M. Liu, H.-R. Wen, S.-J. Liu, F.-Y. Wang and S.-D. Zhu, Multifunctional Dinuclear Dy-Based Coordination Complex Showing Visible Photoluminescence, Single-Molecule

Magnet Behavior, and Proton Conduction, *Inorg. Chem.*, 2022, **61**, 18545.

19 E. Coronado, J. R. Galan-Mascaros, C. J. Gomez-Garcia and V. Laukhin, Coexistence of ferromagnetism and metallic conductivity in a molecule-based layered compound, *Nature*, 2000, **408**, 447.

20 H. Ōkawa, M. Sadakiyo, T. Yamada, M. Maesato, M. Ohba and H. Kitagawa, Proton-Conductive Magnetic Metal–Organic Frameworks, $\{NR_3(CH_2COOH)\}[Ma^{II}Mb^{III}(ox)_3]$: Effect of Carboxyl Residue upon Proton Conduction. H, *J. Am. Chem. Soc.*, 2013, **135**, 2256.

21 D. N. Woodruff, R. E. P. Winpenny and R. A. Layfield, Lanthanide Single-Molecule Magnets, *Chem. Rev.*, 2013, **113**, 5110.

22 Y.-S. Meng, S.-D. Jiang, B.-W. Wang and S. Gao, Understanding the Magnetic Anisotropy toward Single-Ion Magnets, *Acc. Chem. Res.*, 2016, **49**, 2381.

23 C. A. P. Goodwin, F. Ortu, D. Reta, N. F. Chilton and D. P. Mills, Molecular Magnetic Hysteresis at 60 Kelvin in Dysprosocenium, *Nature*, 2017, **548**, 439.

24 F.-S. Guo, B. M. Day, Y.-C. Chen, M.-L. Tong, A. Mansikkamäki and R. A. Layfield, Magnetic hysteresis up to 80 kelvin in a dysprosium metallocene single-molecule magnet, *Science*, 2018, **362**, 1400.

25 Y.-S. Ding, N. F. Chilton, R. E. P. Winpenny and Y.-Z. Zheng, On Approaching the Limit of Molecular Magnetic Anisotropy: A Near-Perfect Pentagonal Bipyramidal Dysprosium(III) Single-Molecule Magnet, *Angew. Chem., Int. Ed.*, 2016, **55**, 16071.

26 Z. Zhu, C. Zhao, T. Feng, X. Liu, X. Ying, X.-L. Li, Y.-Q. Zhang and J. Tang, Air-Stable Chiral Single-Molecule Magnets with Record Anisotropy Barrier Exceeding 1800 K, *J. Am. Chem. Soc.*, 2021, **143**, 10077.

27 R. Sun, C. Wang, B.-W. Wang, Z.-M. Wang, Y.-F. Chen, M. Tamm and S. Gao, Low-coordinate bis(imidazolin-2-iminato) dysprosium(III) single-molecule magnets, *Inorg. Chem. Front.*, 2023, **10**, 485.

28 Z. Zhu, X. Ying, C. Zhao, Y.-Q. Zhang and J. Tang, A new breakthrough in low-coordinate Dy(III) single-molecule magnets, *Inorg. Chem. Front.*, 2022, **9**, 6061.

29 K. Liu, W. Shi and P. Cheng, Toward heterometallic single-molecule magnets: Synthetic strategy, structures and properties of 3d-4f discrete complexes, *Coord. Chem. Rev.*, 2015, **289–290**, 74.

30 C. Aronica, G. Pilet, G. Chastanet, W. Wernsdorfer, J.-F. Jacquot and D. Luneau, A Nonanuclear Dysprosium(III)–Copper(II) Complex Exhibiting Single-Molecule Magnet Behavior with Very Slow Zero-Field Relaxation, *Angew. Chem., Int. Ed.*, 2006, **45**, 4659.

31 F. Mori, T. Nyui, T. Ishida, T. Nogami, K.-Y. Choi and H. Nojiri, Oximate-Bridged Trinuclear Dy−Cu−Dy Complex Behaving as a Single-Molecule Magnet and Its Mechanistic Investigation, *J. Am. Chem. Soc.*, 2006, **128**, 1440.

32 I. A. Kühne, N. Magnani, V. Mereacre, W. Wernsdorfer, C. E. Ansona and A. K. Powell, An octanuclear $\{Cu^{II}_4Dy^{III}_4\}$ coordination cluster showing single molecule magnet behaviour from field accessible states, *Chem. Commun.*, 2014, **50**, 1882.

33 R. Modak, Y. Sikdar, G. Cosquer, S. Chatterjee, M. Yamashita and S. Goswami, Heterometallic Cu^{II}-Dy^{III} Clusters of Different Nuclearities with Slow Magnetic Relaxation, *Inorg. Chem.*, 2016, **55**, 691.

34 C.-M. Liu, D.-Q. Zhang and D.-B. Zhu, Fine Tuning the Energy Barrier of Molecular Nanomagnets via Lattice Solvent Molecules, *Sci. Rep.*, 2017, **7**, 15483.

35 C.-M. Liu, D.-Q. Zhang, X. Hao and D.-B. Zhu, Assembly of chiral 3d-4f wheel-like cluster complexes with achiral ligands: single-molecule magnetic behavior and magnetocaloric effect, *Inorg. Chem. Front.*, 2020, **7**, 3340.

36 A. Bhanja, S. R. Chaudhuri, A. B. Canaj, S. P. Vyas, F. Ortu, L. Smythe, M. Murrie, R. Goswamic and D. Ray, Synthesis and characterization of two self-assembled $[Cu_6Gd_3]$ and $[Cu_5Dy_2]$ complexes exhibiting the magnetocaloric effect, slow relaxation of magnetization, and anticancer activity, *Dalton Trans.*, 2023, **52**, 3795.

37 T. Shiga, H. Miyamoto, Y. Okamoto, H. Oshio, N. Mihara and M. Nihei, Tetranuclear $[Cu_3Ln]$ complexes derived from a tetraketone-type ligand, *Dalton Trans.*, 2023, **52**, 3947.

38 L. Ungur, S.-Y. Lin, J. Tang and L. F. Chibotaru, Single-molecule toroics in Ising-type lanthanide molecular clusters, *Chem. Soc. Rev.*, 2014, **43**, 6894.

39 A. B. Canaj, D. I. Tzimopoulos, M. Siczek, T. Lis, R. Inglis and C. J. Milios, Enneanuclear $[Ni_6Ln_3]$ Cages: $[Ln^{III}_3]$ Triangles Capping $[Ni^{II}_6]$ Trigonal Prisms Including a $[Ni_6Dy_3]$ Single-Molecule Magnet, *Inorg. Chem.*, 2015, **54**, 7089.

40 S. Yu, H.-L. Wang, Z. Chen, H.-H. Zou, H. Hu, Z.-H. Zhu, D. Liu, Y. Liang and F.-P. Liang, Two Decanuclear $Dy^{III}_xCo^{II}_{10-x}$ (x=2, 4) Nanoclusters: Structure, Assembly Mechanism, and Magnetic Properties, *Inorg. Chem.*, 2021, **60**, 4904.

41 C.-M. Liu, R.-G. Xiong, D.-Q. Zhang and D.-B. Zhu, Nanoscale Homochiral C_3-Symmetric Mixed-Valence Manganese Cluster Complexes with Both Ferromagnetic and Ferroelectric Properties, *J. Am. Chem. Soc.*, 2010, **132**, 4044.

42 C. A. Mattei, V. Montigaud, F. Gendron, S. Denis-Quanquin, V. Dorcet, N. Giraud, F. Riobé, G. Argouarch, O. Maury, B. Le Guennic, O. Cador, C. Lalli and F. Pointillart, Solid-state versus solution investigation of a luminescent chiral BINOL-derived bisphosphate single-molecule magnet, *Inorg. Chem. Front.*, 2021, **8**, 947.

43 B.-F. Long, S. Yu, Z.-H. Zhu, Y.-L. Li, F.-P. Liang and H.-H. Zou, Coordination site manipulation of the annular growth mechanism to assemble chiral lanthanide clusters with different shapes and magnetic properties, *Inorg. Chem. Front.*, 2022, **9**, 5950.

44 B. E. Rez, J. Liu, V. Béreau, C. Duhayon, Y. Horino, T. Suzuki, L. Coolen and J.-P. Sutter, Concomitant emergence of circularly polarized luminescence and single-

molecule magnet behavior in chiral-at-metal Dy complex, *Inorg. Chem. Front.*, 2020, **7**, 4527.

45 A. W. Addison, T. N. Rao, J. Reedijk, J. van Rijn and G. C. Verschoor, Synthesis, Structure, and Spectroscopic Properties of Copper(II) Compounds containing Nitrogen-Sulphur Donor Ligands; the Crystal and Molecular Structure of Aqua[l,7-bis(N-methylbenzimidazol-2′-yl)-2,6-dithiaheptane]copper(II) Perchlorate, *J. Chem. Soc., Dalton Trans.*, 1984, 1349.

46 D. Casanova, M. Llunell, P. Alemany and S. Alvarez, The Rich Stereochemistry of Eight-Vertex Polyhedra: a Continuous Shape Measures Study, *Chem. – Eur. J.*, 2005, **11**, 1479.

47 J. A. Mydosh, *Spin Glasses, An Experimental Introduction*, Taylor and Francis Ltd, London, 1993, pp. 1–256.

48 K. S. Cole and R. H. Cole, Dispersion and Absorption in Dielectrics I. Alternating Current Characteristics, *J. Chem. Phys.*, 1941, **9**, 341.

49 S. M. Aubin, Z. Sun, L. Pardi, J. Krzysteck, K. Folting, L.-J. Brunel, A. L. Rheingold, G. Christou and D. N. Hendrickson, Reduced Anionic Mn_{12} Molecules with Half-Integer Ground States as Single-Molecule Magnets, *Inorg. Chem.*, 1999, **38**, 5329.

50 S. Chorazy, J. J. Zakrzewski, M. Reczyński, K. Nakabayashi, S.-I. Ohkoshi and B. Sieklucka, Humidity driven molecular switch based on photoluminescent $Dy^{III}Co^{III}$ single-molecule magnets, *J. Mater. Chem. C*, 2019, **7**, 4164.

51 J. Liu, X.-P. Zhang, T. Wu, B.-B. Ma, T.-W. Wang, C.-H. Li, Y.-Z. Li and X.-Z. You, Solvent-Induced Single-Crystal-to-Single-Crystal Transformation in Multifunctional Chiral Dysprosium(III) Compounds, *Inorg. Chem.*, 2012, **51**, 8649.

52 G. L. J. A. Rikken and E. Raupach, Enantioselective magnetochiral photochemistry, *Nature*, 2000, **405**, 932.

53 Y.-J. Zhang, G. Wu, H. Xu, X. Wang, L.-S. Long, X.-J. Kong and L.-S. Zheng, Magnetooptical Properties of Chiral $[Co_2Ln]$ Clusters, *Inorg. Chem.*, 2020, **59**, 193.

54 Y. Kitagawa, S. Wada, K. Yanagisawa, T. Nakanishi, K. Fushimi and Y. Hasegawa, Molecular Design Guidelines for Large Magnetic Circular Dichroism Intensities in Lanthanide Complexes, *ChemPhysChem*, 2016, **17**, 845.

55 X. X. Xie, Y. C. Yang, B. H. Dou, Z. F. Li and G. Li, Proton conductive carboxylate-based metal-organic frameworks, *Coord. Chem. Rev.*, 2020, **403**, 213100.

56 S. M. Elahi, S. Chand, W. H. Deng, A. Pal and M. C. Das, Polycarboxylate-Templated Coordination Polymers: Role of Templates for Superprotonic Conductivities of up to 10^{-1} S cm^{-1}, *Angew. Chem., Int. Ed.*, 2018, **57**, 6662.

57 S. S. Bao, G. K. H. Shimizu and L. M. Zheng, Proton conductive metal phosphonate frameworks, *Coord. Chem. Rev.*, 2019, **378**, 577.

58 Y. Ye, L. Q. Zhang, Q. F. Peng, G. E. Wang, Y. C. Shen, Z. Y. Li, L. H. Wang, X. Y. Ma, Q. H. Chen, Z. J. Zhang and S. C. Xiang, High Anhydrous Proton Conductivity of Imidazole-Loaded Mesoporous Polyimides over a Wide Range from Subzero to Moderate Temperature, *J. Am. Chem. Soc.*, 2015, **137**, 913.

59 Y. S. Wei, X. P. Hu, Z. Han, X. Y. Dong, S. Q. Zang and T. C. W. Mak, Unique Proton Dynamics in an Efficient MOF-Based Proton Conductor, *J. Am. Chem. Soc.*, 2017, **139**, 3505.

60 W. L. Xue, W. H. Deng, H. Chen, R. H. Liu, J. M. Taylor, Y. K. Li, L. Wang, Y. H. Deng, W. H. Li, Y. Y. Wen, G. E. Wang, C. Q. Wan and G. Xu, MOF-Directed Synthesis of Crystalline Ionic Liquids with Enhanced Proton Conduction, *Angew. Chem., Int. Ed.*, 2021, **60**, 1290.

61 H. Gao, Y.-X. Wang, Y.-B. He and X.-M. Zhang, Sequential enhancement of proton conductivity by aliovalent cadmium substitution and post-synthetic esterolysis in a carboxylate-functionalized indium framework with dimethylaminium templates, *Inorg. Chem. Front.*, 2022, **9**, 2997.

62 Q. Qiao, H.-J. Wang, C.-P. Li, X.-Z. Wang and X.-M. Ren, Improving proton conduction of the Prussian blue analogue $Cu_3[Co(CN)_6]_2{\cdot}nH_2O$ at low humidity by forming hydrogel composites, *Inorg. Chem. Front.*, 2021, **8**, 2305.

63 X.-Q. Ji, R. Sun, J. Xiong, H.-L. Sun and S. Gao, Tuning the dynamic magnetic behaviour and proton conductivity via water-induced reversible single-crystal to single-crystal structural transformation, *J. Mater. Chem. C*, 2021, **9**, 15858.

64 C. Si, P. Ma, Q. Han, J. Jiao, W. Du, J. Wu, M. Li and J. Niu, A Polyoxometalate-Based Inorganic Porous Material with both Proton and Electron Conductivity by Light Actuation: Photocatalysis for Baeyer–Villiger Oxidation and Cr(VI) Reduction, *Inorg. Chem.*, 2021, **60**, 682.

65 J.-J. Hu, Y.-G. Li, H.-R. Wen, S.-J. Liu, Y. Peng and C.-M. Liu, Stable Lanthanide Metal–Organic Frameworks with Ratiometric Fluorescence Sensing for Amino Acids and Tunable Proton Conduction and Magnetic Properties, *Inorg. Chem.*, 2022, **61**, 6819.

66 X.-N. Zhang, B.-C. Chen, J.-L. Zhang, J.-L. Zhang, S.-J. Liu and H.-R. Wen, Anionic lanthanide metal–organic frameworks with magnetic, fluorescence, and proton conductivity properties and selective adsorption of a cationic dye, *Dalton Trans.*, 2022, **51**, 15762.

67 X. N. Zou, D. S. Zhang, Y. L. Xie, T. X. Luan, W. C. Li, L. Li and P. Z. Li, High Enhancement in Proton Conductivity by Incorporating Sulfonic Acids into a Zirconium-Based Metal-Organic Framework via "Click" Reaction, *Inorg. Chem.*, 2021, **60**, 10089.

68 P. Tholen, C. A. Peeples, R. Schaper, C. Bayraktar, T. S. Erkal, M. M. Ayhan, B. Çoşut, J. Beckmann, A. O. Yazaydin, M. Wark, G. Hanna, Y. Zorlu and G. Yücesan, Semiconductive microporous hydrogen-bonded organophosphonic acid frameworks, *Nat. Commun.*, 2020, **11**, 3180.

